Spatial Deconvolution of 3-D Diffuse Optical Tomographic Time Series: Influence of Background Medium Heterogeneity

Y. Xu[1,2], H. L. Graber[1,2], Y. Pei[2], R. L. Barbour[1,2]

[1]Dept. of Pathology / SUNY Downstate Medical Center / 450 Clarkson Ave. Brooklyn, NY 11203; yong_xu@downstate.edu

[2]NIRx Medical Technologies LLC / 15 Cherry Lane / Glen Head, NY 11545

INTRODUCTION

We have previously shown that linear convolution of spatial information is the principal cause of the relatively low spatial resolution and quantitative accuracy of DOT images reconstructed by linear perturbation approaches [1]. A deconvolution algorithm was developed that was shown to significantly improve qualitative and quantitative image accuracy, with a computational effort that is negligible compared to recursive iterative reconstruction techniques [2-5].

A potential limitation of the earlier work is that it examined only cases where the target medium consisted of a number of convex inclusions embedded in a homogeneous background. Left open is the possibility that the positive results obtained are sensitive to the spatial extent of the mismatch between the optical parameters of the medium used for generating a deconvolution operator, or filter, and those of the medium to which the filter is subsequently applied. Similarly, the effectiveness of deconvolution might be sensitive to increasingly complex parameter spatial distributions, or to increasingly irregular external geometries. Here we present results of our examinations of these issues.

METHODS

The starting point for the geometrical model used here was a 3D T1-weighted structural MRI of the human head. The section shown in Figure 1, which lies at the level of the temporal bone to the mid-mandible and has a maximal horizontal total width of ~12.5 cm, intersects the pre-motor and primary motor cortices. The region indicated by a red outline (~6 cm along the surface, 3 cm in depth), whose dimensions are typical of those of the tissue volume we interrogate in a dynamic DOT brain study, was chosen as the basis of a heterogeneous target medium for simulation studies. Seven principal tissue types—scalp, muscle, skull, cerebrospinal fluid (CSF), gray matter, and white matter—were identified within the selected area, the interfaces between them, as well as the exterior boundary, were traced. A 2D finite element model was created, taking the selected region's borders and inter-tissue-type interfaces as the boundaries of surface sub-regions. Next, a model with 3D geometry was generated by extruding the 2D model in the orthogonal direction, producing the cylinder depicted in Figure 2(a). Finally, an additional small sub-volume was created within the "gray matter" region of the 3D model, having no boundary in common with the model's external surfaces, as shown in Figure 2(b). Optical coefficient values can be assigned to each sub-region independently; thus the last volume added can be interpreted either as the portion of cerebral cortex that is activated by a specific task, or as a tumor or other lesion.

Shown in Fig. 2(a) are the 25 simulated source and detector locations for the simulated DOT measurements reported on here. The array depicted closely approximates the arrangement of optical fibers typically used in performing finger-tapping studies or other measurements of hemodynamics associated with specific activations of the pre-motor and/or primary motor cortices.
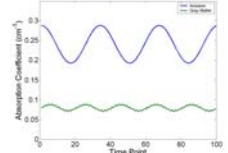
All surface detector data and internal photon intensities (the latter needed for computation of the transformation matrices used in image reconstruction [6]) were obtained by performing finite element method (FEM) computations to numerically solve the diffusion equation with Robin boundary conditions [7]. Each forward-problem computation was performed four times, once for each of the four values of μ_a assigned to the CSF (Table 1).

Sinusoidal temporal variation (Figure 3) was imposed on the absorption coefficient in two of the model tissue compartments, allowing us to evaluate the impact of all mathematical operations on the recoverability of dynamic information. The inclusion volume and the gray matter in which the inclusion is embedded were the regions considered for this purpose. Also, images were reconstructed from data that were either noise free, or were contaminated with white Gaussian additive noise (see Fig. 6). Elementary temporal and spatial low-pass filtering techniques were applied, after the reconstruction and deconvolution steps [5], to assess the extent to which the effect of noise is reversible.

Deconvolution operators and detector-readings time series were computed for four time-averaged optical parameters (Table 1). To examine the sensitivity of the image enhancement algorithm to a spatially complex mismatch between the optical parameters of the filter-generating and target media, every deconvolution operator was applied to the images reconstructed from each medium's detector data. Spatial and temporal correlations (SC and TC, respectively) were computed, between the true properties of each target medium and all corresponding image time series.
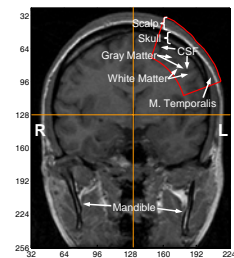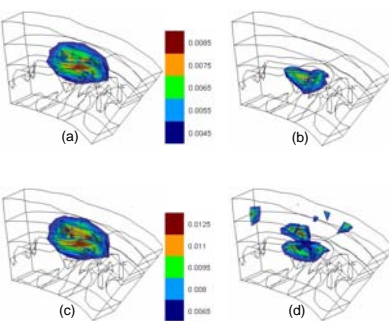

Figure 1. Coronal section of a 3D T1-weighted structural MRI of the human head, that was the starting point for the heterogeneous target medium use in this report's simulation studies. The section shown intersects the pre-motor and primary motor cortices.


Figure 2. (a) Exterior view of the 3D model geometry generated from the MRI section shown in Fig. 1; source and detector positions also are indicated, as small white circles. (b) Interior view of the 3D model from Fig. 2(a), revealing the inclusion embedded in the gray-matter zone.

Figure 3. Plots of μ_a vs. time, in the inclusion and gray-matter compartments of the 3D tissue model of Fig. 2(b),(c).

Table 1. Optical coefficient values (for tissue types with dynamic μ_a, tabulated number is the temporal mean) assigned to the different tissue compartments of the MRI-based 3D geometry, for all target (Case1-4) and reference (Filter1-4) media that were modeled.

	CSF		Inclusion		Others	
	μ_s (cm^{-1})	μ_a (cm^{-1})	μ_s (cm^{-1})	μ_a (cm^{-1})	μ_s (cm^{-1})	μ_a (cm^{-1})
Case1	10.0	0.080				
Case2	5.0	0.040				
Case3	1.0	0.010	10.0	0.24	10.0	0.08
Case4	0.5	0.005				
Filter1	10.0	0.080				
Filter2	5.0	0.040				
Filter3	1.0	0.010	10.0	0.08		
Filter4	0.5	0.005				

Figure 4. Volume rendering of the Fig. 2(b) target medium. (a) Case1 detector data, Filter2 reference medium (see Table 1), before deconvolution. (b) Case1 detector data, Filter2 reference medium, after deconvolution. (c) Case3 detector data, Filter2 reference medium (see Table 1), before deconvolution. (d) Case3 detector data, Filter2 reference medium, after deconvolution. In each sub-figure, the range of μ_a values plotted runs from $\mu_a^{max}/2$ to μ_a^{max}.
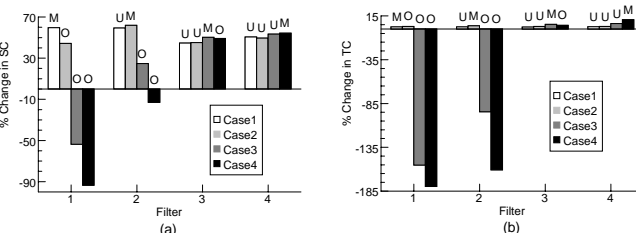
Figure 5. (a) Bar graph of relative percent change in image spatial correlation, comparing the image-to-target SC after and before spatial deconvolution, for all 16 Case/Filter pairings. (b) Bar graph of the corresponding relative percent changes in image temporal correlation. Annotations above bars indicate whether the reference-medium CSF optical coefficients match ('M'), over-estimate ('O') or under-estimate ('U') those of the target medium
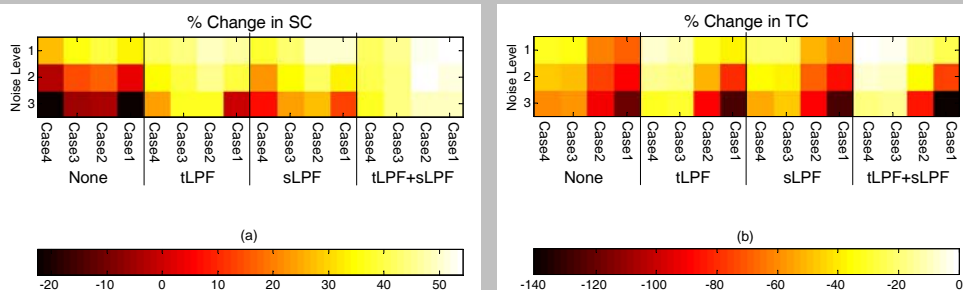
RESULTS

Spatially convolved images are shown in Fig. 4(a),(c); the Fig. 4(a) result, Case1/Filter2, is computed using a weight function that under-estimates the CSF optical coefficients, while the Case3/Filter2 image [Fig. 4(c)] is obtained when weight functions are used that over-estimate the CSF optical coefficients. The noteworthy features of Figs. 4(a),(c) are: they are qualitatively very similar; there is substantial depth location error, with the recovered μ_a perturbation apparently located within the skull; the size of the inclusion is over-estimated in all cases; the magnitude of the μ_a perturbation is under-estimated in all cases.

Qualitative image accuracy is more variable after spatial deconvolution than before. The result obtained for the Case1/Filter2 pairing is, as shown in Fig. 4(b), superior to the Fig. 4(a) result in the three important respects of depth location, inclusion size, and quantitative perturbation magnitude. In stark contrast, when the direction of the mismatch is reversed and the CSF optical coefficients are over-estimated [Fig. 4(d)], the high-absorption region of the deconvolved image splits into two parts, one still at the correct location and the other consisting of superficial artifacts. Increasing the magnitude of the mismatch leads to a completely erroneous result (not shown) that consists almost exclusively of the superficial artifacts. Comparison of imaging results for all 16 Case/Filter pairings and all 100 time frames show that the type of trend seen in Fig. 4 turns up consistently.

The effect of deconvolution was quantified by computing the relative differences between the SC and TC values vs. before this procedure. The percent changes, for all 16 Case/Filter pairings, are plotted in Figure 5(a) (spatial) and 5(b) (temporal). The white bars are data for the Case1 medium, for which the CSF optical coefficients are never over-estimated; it is seen that deconvolution always brings about an increase in SC and TC. The black bars are data for the Case4 medium, for which the CSF optical coefficients are never under-estimated; it is seen that effect of deconvolution ranges from significant degradation of image quality to substantial improvement. Results for the other Cases are intermediate those for the preceding two.

Figure 6 shows the percent changes in SC [Fig. 6(a)] and TC [Fig. 6(b)], for all four CaseN/Filter3 pairings and all three noise levels. As in Fig. 5, positive(negative) values indicate that the correlation is higher(lower) after deconvolution than before. Inspection shows that: at the lowest noise level, which is typical of data collected in DOT brain measurements: 1) the SC invariably increases upon spatial deconvolution; 2) the loss of TC associated with deconvolution can be minimized by using sLPF and tLPF in combination.

CONCLUSIONS

The trend noted in Figs. 4,5 is readily explicable, and it does not cast doubt upon the utility of the deconvolution algorithm; the error-inducing situation is easily avoided in practice. The straightforward explanation for the asymmetric dependence of artifact on mismatch is that weight matrices computed for media with lower μ_s and μ_a values in the CSF assign greater importance to the regions lying deep to it, which in our model includes the inclusion sub-volume.

The practically significant conclusions of the noise studies are that, irrespective of the noise level: 1) the percentage increase in SC can be made larger by using LPFs, especially sLPF and tLPF in combination; 2) the loss of TC can be held to acceptable levels, provided that the reference-medium CSF optical coefficients do not over-estimate those of the target medium.

REFERENCES

1. H.L. Graber, R.L. Barbour, and Y. Pei, "Quantification and enhancement of image reconstruction accuracy by frequency encoding of spatial information," in *OSA Biomedical Topical Meetings, OSA Technical Digest* (Optical Society of America, Washington DC, 2002), pp. 635-637.

2. R.L. Barbour, H.L. Graber, Y. Xu, Y. Pei, and R. Aronson, "Strategies for imaging diffusing media," *Transport Theory and Statistical Physics* **33**: 361-371 (2004).

3. H.L. Graber, Y. Xu, Y. Pei, and R.L. Barbour, "Spatial deconvolution technique to improve the accuracy of reconstructed three-dimensional diffuse optical tomographic images," *Applied Optics* **44**: 941-953 (2005).

4. Y. Xu, H.L. Graber, Y. Pei, and R.L. Barbour, "Improved accuracy of reconstructed diffuse optical tomographic images by means of spatial deconvolution: two-dimensional quantitative characterization," *Applied Optics* **44**: 2115-2139 (2005).

5. Y. Xu, Y. Pei, H.L. Graber, and R.L. Barbour, "Image quality improvement via spatial deconvolution in optical tomography: Time-series imaging," *J. Biomedical Optics* **10**: 051701 (2005).

6. H.L. Graber, J. Chang, and R.L. Barbour, "Imaging of multiple targets in dense scattering media," *Experimental and Numerical Methods for Solving Ill-Posed Inverse Problems: Medical and Nonmedical Applications*, SPIE Vol. 2570, pp. 219-234 (1995).

7. Y. Pei, H.L. Graber, and R.L. Barbour, "Influence of systematic errors in reference states on image quality and on stability of derived information for DC optical imaging," *Applied Optics* **40**: 5755-5769 (2001).

Figure 6. (a) Colormap of relative percent change in image spatial correlation, comparing the image-vs.-target SC after and before spatial deconvolution, for the four CaseN/Filter3 pairings, three noise levels, and four varieties of noise suppression. (b) Colormap of the corresponding relative percent changes in image temporal correlation. We used a noise model in which, for each source-detector channel, the standard deviation of the noise distribution is a pre-selected percentage of the noise-free detector reading and grows as the fourth power of the distance between source and detector [5]. The minimal noise level (source and detector co-located) was 1, 2 or 3%, while the maximal noise level was, respectively, 10, 20 or 30%.